Minyard, M., Bruns, M. A., Liermann, L. J., Buss, H. L., & Brantley, S. L. (2012). Bacterial associations with weathering minerals at the regolith-bedrock interface, Luquillo Experimental Forest, Puerto Rico. Geomicrobiology Journal, 29(9), 792-803. 10.1080/01490451.2011.619640

Bacterial associations with weathering minerals at the regolith-bedrock interface, Luquillo Experimental Forest, Puerto Rico

Journal:	*Geomicrobiology Journal*
Manuscript ID:	UGMB-2011-0097
Manuscript Type:	Original Article
Date Submitted by the Author:	18-Aug-2011
Complete List of Authors:	Bruns, Mary Ann; The Pennsylvania State University, Department of Crop and Soil Sciences Minyard, Morgan; The Pennsylvania State University, Crop and Soil Sciences Liermann, Laura; The Pennsylvania State University, Geosciences Buss, Heather; University of Bristol, School of Earth Sciences Brantley, Susan; The Pennsylvania State University, Geosciences
Keywords:	subsurface microbiology, molecular ecology, iron oxidation

ABSTRACT

Microbe-mineral associations in regolith overlying granodiorite bedrock (4.6-4.9 m depth) from the Luquillo Experimental Forest, Puerto Rico, were imaged with confocal scanning laser microscopy at a novel scale of 400X magnification. After adding BacLight™ stain, proportionally more surface area of minerals (quartz, biotite, and mixed opaque kaolinite/goethite) emitted fluorescence from cell-impermeant propidium iodide than from cell-permeant SYTO 9, which suggested greater coverage of minerals by extracellular DNA or DNA in non-intact cells than by intact cells. Microscopic observations of predominantly non-intact cell material in deep saprolite were consistent with the abundance of rRNA sequences related to heterotrophic bacteria in clone libraries prepared from community DNA. A few sequences were affiliated with bacteria recognized to produce siderophores, oxidize Fe(II), or fix N_2. Bacterial DNA in deep regolith from two boreholes 1.5 m apart yielded libraries with high diversity and taxa specific for each borehole.

INTRODUCTION

Bedrock weathering in the Rio Icacos watershed of the Luquillo Experimental Forest (LEF) in eastern Puerto Rico accounts for one of the highest documented weathering rates for granitic rock in the world (McDowell and Asbury 1994; White and Blum 1995; Braun et al. 2005). Explanations for the very high weathering rates include enhanced chemical weathering by high annual rainfall (4200 mm average) and high soil temperatures (annual mean of 22 ºC) (USDA NCRS 2002), as well as by reaction-induced fracturing of bedrock (Buss et al. 2008). Increased bacterial densities observed at the interface between bedrock and regolith, however, suggest that microbiological processes also contribute to weathering in the LEF (Buss et al. 2005).

Regolith in the Rio Icacos watershed is derived from bedrock corestones of the Rio Blanco stock, an early Tertiary age intrusion of quartz diorite (Seiders 1971) composed mainly of plagioclase (56%) and quartz (25%) with smaller proportions of biotite (9%), hornblende (6%), K-feldspar (2%), and goethite (2%) (Murphy 1995; White et al. 1998). These bedrock corestones weather "spheroidally" (Fritz and Ragland 1980), so that their outermost portions exhibit characteristic concentric layers, or "rindlets" of partially weathered rock (Turner et al. 2003; Buss et al. 2005; Fletcher et al. 2006; Buss et al. 2008). Weathering of regolith that develops from these corestones has been studied extensively on Guaba Ridge in the LEF (White et al. 1998; Murphy et al. 1998; Dong et al. 1998; Schulz and White 1999; Turner et al. 2003). The upland regolith consists of a layer of surface soil (0-0.5 m), a transition layer (0.5-1.1 m) and a variably thick (5-8 m) layer of saprolite, defined as a "clay-rich, chemically weathered rock altered in place to retain the structure and volume of the parent rock" (American Geological Institute 1976).

Saprolite below the rooting zone (> 0.6-0.8 m) is inherently low in organic carbon (~0.1%), yielding no more than 10^{3-4} colony-forming units of aerobic heterotrophs per gram (Buss et al., 2005). Major saprolite components are secondary kaolinite (57-63%) and goethite (2-4%), as well as persistent grains of primary quartz (21-24%) and oxidized biotite (16-21%) (Murphy et al. 1998; White et al. 1998; Buss et al., 2008). Whereas most of the saprolite layer would be an unfavorable, low-nutrient environment for microbial proliferation, deep saprolite immediately above bedrock may offer better conditions for microbial survival and possibly growth of lithoautotrophs. Microbes in deepest saprolite would have greatest access to the fluxes of minerals from a thin, interface layer of "saprock" (ca. 7 cm) that lies between the saprolite and corestone rindlets (Buss et al., 2008).

We use the term "saprock" here to indicate the material between saprolite and bedrock rindlets. This layer has also been described as "protosaprolite" and is distinguished by its greater porosity and lower mechanical strength than underlying rindlets, but it is not as fully disaggregated nor as plastic as the saprolite above it (Buss et al. 2010). In this layer, hornblende, plagioclase and K-feldspar are completely converted to kaolinite and goethite, and apatite is completely dissolved (White et al. 1998; Buss et al., 2010). Using the observed weathering rate for complete alteration of hornblende across the saprock layer, the estimated rate of release of Fe(II) at steady-state was calculated to be sufficient to support C assimilation by 10^{4-5} Fe(II)-oxidizing bacteria cells g^{-1} in saprolite above the saprock (Buss et al., 2005).

In a previous study, the deepest (> 4.6 m) saprolite samples from a 5 m-thick regolith at the Luquillo-Guaba (LG-1) study site exhibited 100-fold higher direct microscopic counts (10^{9} cells g^{-1}), culturable aerobic heterotrophs (10^{5-7} cfu g^{-1}), and extractable microbial

community DNA (10 µg g^{-1}) compared to numbers observed in overlying saprolite (Buss et al., 2005). Microbial densities were not correlated with organic carbon content or total Fe but were correlated with moisture content and HCl-extractable Fe(II).

For the present study, we obtained deep saprolite and saprock samples from the bases of two additional boreholes at the LG-1 site. Our objectives were to gain insights into microbial distribution on the surfaces of non-enriched, native mineral grains using microscopic methods and to analyze microbial community DNA extracted from the samples with 16S rRNA clone libraries. To our knowledge, this is the first molecular analysis of bacterial community composition in deep tropical saprolite. We were specifically interested in detecting Fe(II)-oxidizing bacteria, which could enhance primary mineral dissolution at the bedrock-regolith interface, and in the degree of spatial variability of bacterial community structure.

METHODS

Site Description and Sample Collection.

The 326-ha Rio Icacos watershed in the Luquillo Mountains of eastern Puerto Rico consists of steep rugged terrain dominated by lower montane wet Colorado forest (Brown et al. 1983). Chemical weathering and solute transport in this watershed have been described in many previous reports (e.g. Larsen et al. 1993; White et al. 1998; Stonestrom et al. 1998; Murphy et al. 1998; Schulz and White 1999; Turner et al. 2003; Buss et al. 2008; Buss et al. 2010). For the present study, two boreholes were manually augered through soil and saprolite on Luquillo's Guaba Ridge at an upland shoulder location (site LG-1), elevation 680 m, latitude 18° 16' 54.2"N, longitude 65° 47' 25.3"W. Soil on the Guaba Ridge is an inceptisol belonging to the Picacho-Ciales complex, a very deep, poorly drained soil classified as a fine

loamy, kaolinitic, isothermic Aquic Dystrudepts (USDA NRCS 2002). This soil has a thin A horizon (< 0.1 m) and a weakly developed, clay-enriched Bw horizon above a 4- to 8-m layer of saprolite. Beneath the saprolite is a thin (7-cm) layer of friable saprock above another layer (0.5-2 m) of concentric rindlets at the outer edges of spheroidally weathering corestones (Buss et al. 2008). Rindlets are curved slabs of bedrock separated by fractures about 2 cm apart (Fletcher et al., 2006). Pore water pH measurements throughout the regolith profile have ranged from 4.0 – 5.4 (White et al. 1998).

Two cores, designated LG-1 N(orth) and LG-1 S(outh), were collected 1.5 m apart. The auger bucket was driven into the regolith to bring a core section to the surface at 15-cm intervals. Soil and saprolite samples (approx. 200 g) were collected from core sections at selected depths. For aseptic sampling, outer core material was removed and the inner portions of selected core sections were placed in sterile plastic bags. After mixing, subsamples for direct microscopic examination were placed in 4% formaldehyde immediately to preserve shape and structure of resident microbial cells (Murray et al. 1994). After removal of each core section, the empty bucket was lowered back into the borehole, and these steps were repeated until manual augering could penetrate no further, indicating that denser saprock had been reached (4.88 m for LG-1 N core and 4.80 m for LG-1 S core). To collect saprock samples, a bulk density sampler ring (5.7 cm diameter and 7 cm height) attached to the bottom of a 6-m pole was lowered to the bottom of each borehole. By hammering the top of the pole, the sampler ring was pounded down to a depth of 7 cm, after which it was pulled up to the surface. The sampler ring was carefully separated from the pole and capped for shipping. Saprock cores were kept intact (neither mixed nor fixed) for

shipment on ice, with the soil and saprolite samples, to the Pennsylvania State University within four days.

Confocal Laser Scanning Microscopy (CLSM)

Preserved sample preparation

Samples of formaldehyde-fixed regolith were obtained from 12 different depths of each core, where zero-depth was defined as the interface between organic soil and mineral soil at the surface (Table 1). Samples were weighed (0.2 -0.4 g) into small petri dishes (6 cm diameter) and mixed with 2 ml sterile 2% molten agarose (45°C) to create an evenly distributed suspension in the dish. Discs (34.9 mm^3, 7.50 mm diameter, 0.8 mm height) were cut from solidified agarose and placed onto the coverglass of a Lab-Tek® chamber (Nalgene Nunc, Rochester, NY). The edges of each disk were fixed to the coverglass with an additional 25 µL of molten agarose. Analysis by CLSM occurred within 3 hours of preparation of the disks.

CLSM procedures

Three illumination channels were used to collect images of mineral grains and associated microorganisms with an Olympus FluoView 300 CLSM microscope (Melville, NY). Visible light from the differential interference contrast (DIC) channel provided gray-scale images of the lower surfaces of mineral grains suspended in transparent agarose (Suppl. Fig. 1). To visualize cells, two laser channels provided 488-nm light from a blue argon (Ar) laser and 543-nm light from a green helium-neon (HeNe) laser for excitation of SYTO 9 and propidium iodide, respectively, in the *Bac*Light stain (Molecular Probes Inc, Eugene, OR).

The chambered coverglass holding agarose disks was placed on the microscope stage above the inverted objective for manual focusing on mineral grains nearest the coverglass

using the DIC channel (Suppl. Fig. 1). Prior to staining, agarose disks containing mineral grains were examined under laser excitation to confirm absence of autofluorescence. Without moving the coverglass, discs were stained with 10 µL of 1:10 dilution of *Bac*Light reagent in sterile phosphate-buffered saline. DIC imaging then was used to focus on grains nearest the coverglass, after which the microscope objective, controlled by FluoView v. 1.6 software (Melville, NY), moved upward (z-direction) to capture sequential images (optical sections) in 1.35-µm intervals (height of 27 µm). This interval, slightly greater than the average diameter of a bacterial cell, was used to minimize double counting of cells. For each sample observed, 20 optical sections were combined to create a "z-stack" that provided observation over a total field-of-view (FOV) of 132,400 μm^2. At least six sets (z-stacks) of optical sections were taken for each regolith depth (i.e. total FOV per depth = 6 x 132,400 um^2).

Filters were 510 nm long pass and 530 nm short pass (Ar laser) and 565 nm long pass (HeNe laser). Photomultiplier tube (PMT) and other settings were 756V PMT, 2.2 gain, and 3-4% offset (HeNe); 775V PMT, 1.6X gain, and 4% offset (Ar) and 389V PMT, 1.2X gain, and 3% offset (DIC). All images were captured using 400X magnification (Uplan FL 40X, n.a. 0.75, and 10X ocular). This permitted detection of individual cells and collection of data from larger, more representative fields-of-view (132,400 μm^2) than could be collected at higher magnifications.

Digital image processing

The COMSTAT program, operated in MATLAB, was used to process fluorescent signals from the composite field-of-view through 20 optical sections (Heydorn et al., 2000). The Ar and HeNe laser channels, respectively, were used to track fluorescence from cell-permeant SYTO 9 (when bound to DNA in intact and nonintact cells) and cell-impermeant

propidium iodide (when bound to DNA in nonintact cells or extracellular DNA) (Leuko et al. 2004). Areas occupied by intact and nonintact cells in each composite image were determined by first applying the LOOKTIF tool to the color laser display images and generating black-and-white output files at different threshold values. By comparing output files to the original color display images, the threshold value that best differentiated fluorescent pixels from background pixels was determined. Next, the black-and-white image generated at this threshold value was provided to COMSTAT for calculation of percent area occupied by intact or nonintact cells in the display image (Fig. 1).

The manual selection tool in ImageJ software (National Institute of Health, Bethesda, MD) was applied to the composite image from the DIC channel to quantify areas corresponding to different mineral surfaces. As shown in Fig. 1e, some portions of larger quartz grains were located behind opaque minerals. Only areas of exposed surfaces facing the microscope operator were counted. Selected areas were summed and divided by the FOV area to calculate percentage occupied by biotite; mixed opaque minerals; and transparent quartz. Prior to image analyses, DIC images of known quartz and biotite specimens were compared to minerals in the composite images.

Percent Mineral Surface Area Covered by Cells (%MAC)

For each composite image, we calculated percentage of "mineral cross-sectional area covered by intact cells" (intact %MAC) and percentage of "mineral cross-sectional area covered by nonintact cells" (nonintact %MAC). These percentages were calculated by dividing the area occupied in the image by intact or nonintact cells by the area in the image occupied by total minerals:

$$\%MAC = \frac{\%AreaOccupiedbyCells(Intact\_or\_NonIntact)}{\%AreaOccupiedbyTotalMinerals} \times 100 \quad (1).$$

All COMSTAT and DIC image data were shown to have normal distributions using the statistical software Minitab ($\alpha = 0.05$; State College, PA), except for one outlier image which was removed from the 3.1-m dataset before calculating %MAC at that depth. The Minitab basic statistics function was used to evaluate differences between means of %MAC at adjacent depths (2-sample t-test, $\alpha = 0.05$). Because mineral surface areas per 100,000 μm^2 of field of view examined at different depths varied, areas occupied by each mineral type and by intact and nonintact cells were normalized. The linear regression function in Minitab also was used to determine relationships between cells and mineral areas using default settings and $\alpha = 0.05$. Reported values represent mean from each depth in the regolith profile.

Bacterial Community DNA Analysis

Microbial community DNA was extracted from subsamples of the three deepest core sections from each borehole. Three 5-g amounts of each saprolite sample (4.6 and 4.7 m depths) were extracted according to the methods of Zhou et al. (1996) with three successive extractions that were pooled for 16S rRNA clone library construction. Due to the small amount of saprock samples (4.9 m depth), DNA was extracted from duplicate 0.2 - 0.3 g samples using a PowerSoil DNA extraction kit from MoBio (Carlsbad, CA) and pooled for PCR.

Duplicate PCR reactions (50 µl) were prepared using 5 U *Taq* polymerase (Gene Choice, Frederick, MD), standard buffer, 3.5 mM $MgCl_2$, 0.25 mM dNTPs, 10 pmol of each primer, 0.5 mg $reaction^{-1}$ of bovine serum albumin, and 4 µL of DNA extract per reaction. Temperature cycling consisted of initial denaturation for 5 min at 94°C; 35 cycles of 94 °C-30s/54 °C-30s/ 72 °C-60s; and a final extension of 7 min at 72°C. Universal bacterial primers 27F (5'-AGAGTTTGATCMTGGCTCAG -3') and 907R (5'–

CCCCGTCAATTCMTTTGAGTTT-3') were used to amplify bacterial 16S rRNA genes (Lane 1991). Duplicate reaction mixtures were pooled prior to ligation with a pCR® 4-TOPO vector (Invitrogen, Carlsbad, CA). Plasmids were cloned into TOPO TA chemically competent DH5α-T1 *Escherichia coli* TOP10 cells (Invitrogen). Sequences were checked for chimeras using Greengenes with Bellepheron vs. 3 (DeSantis et al., 2006b). A total of 269 sequences were assigned to taxa using the Ribosomal Database Project (RDP) classifier (Cole et al., 2009). DNA similarities between regolith sequences and closest relatives are reported in this paper as RDP DNAML identification scores (Suppl. Table 1) or percent similarities from pairwise alignments using the Basic Local Alignment Search Tool (BLAST) in GenBank (Altschul et al., 1990).

Sequences were analyzed using DOTUR and LIBSHUFF programs in mothur (Schloss et al. 2009). Sequences were aligned against a comparison library from Greengenes (DeSantis et al. 2006a; DeSantis et al. 2006b), and distance matrices were calculated using mothur. Distance matrices also were used to estimate library coverage for communities at three depths in each borehole (6 libraries total) as well as to evaluate statistical significance of library differences. To estimate community coverage, sequences were first sorted by DOTUR into operational taxonomic units (OTUs) based on $\geq$ 97% sequence similarity. We divided the number of OTUs by the Chao 1-estimated number of OTUs, also at $\geq$ 97% similarity. Chao 1 OTU estimation was chosen over other estimator values because of our relatively small library sizes. When analyzing the libraries for statistical similarities in LIBSHUFF, we used corrected P-values of 0.0085 when comparing the three communities sampled from a single borehole and 0.0017 when comparing all six communities (Schloss et al. 2009).

Genbank accession numbers for 16S rRNA gene sequences are HQ445627 to HQ445898.

RESULTS

Microscopic observations of mineral grains, cells, and biofilms

Quartz and biotite could be readily identified in DIC images by their relatively large grain sizes, as they are the two major primary minerals in Guaba Ridge saprolite (Murphy et al., 1998; White et al., 1998). Quartz grains were distinguishable by their transparency and sharp, angular edges (labeled Q in Fig. 1f), while biotite was observed as larger (>100 µm) opaque, cracked grains with laminar structure and separating edges (labeled B in Fig. 1f). The third mineral class consisted of mixed opaque grains or aggregates (< 50 µm) that could not be identified as biotite (labeled M in Fig. 1f). Based on previous mineralogical studies, mixed opaque minerals could be either goethite, kaolinite, halloysite, or heavily coated, highly weathered primary minerals (Dong et al. 1998; Murphy et al. 1998; White et al. 1998). Areas corresponding to the three mineral classes, as outlined in DIC images (Fig. 1f), were used to calculate percentages of field occupied by each mineral class. Total surface areas of grains examined at each depth ranged from 75,877 to 620,255 μm^2 (Table 1).

Under laser illumination, green fluorescence emitted from SYTO 9 was typically observed as discrete points, 1-3 μm^2 in area, which appeared to be individual intact cells or multiples of 2-4 cells (Fig. 2). Irregularly shaped patches emitting red fluorescence from the nonintact cell stain propidium iodide (Fig. 2) were larger in area (up to 5000 μm^2 or more), and generally followed the outlines of the mineral surfaces with which they were associated. These irregular and discontinuous areas of red fluorescence were interpreted to be biofilms consisting of extracellular polysaccharides and other organic material entrapping

extracellular DNA or DNA in nonintact cells. Discrete points of green fluorescence were sparsely distributed in red-fluorescing biofilms. In Fig. 1b and 1d, intact and nonintact cells occupied 0.015% and 1.84%, respectively, of image area, as calculated by COMSTAT (Heydorn et al., 2000).

Cell-mineral associations were evaluated in four depth intervals of the regolith: i) soil (Bw) at 0.15 and 0.31 m; ii) upper saprolite at 1.5-2.0 m; iii) Mn-rich saprolite at 2.4 m, which was previously identified as a "ghost rindlet" that had not transformed entirely to saprolite but retained some saprock character (Buss et al., 2005); iv) and lower saprolite at 3.1-4.7 m (Table 1). Areas viewed for total minerals, intact cells and nonintact cells were greatest in the soil samples, which were more weathered and aggregated than saprolite. In the two depths investigated in the upper saprolite, 1.5 and 2.0 m, the mean %MAC values at each depth for intact cells (3.6 and 1.9 %, respectively) and nonintact cells (17.0 and 4.1 %MAC, respectively) were higher than in lower saprolite (means ranging from 0.04-0.88% and 0.57-5.94% for intact and nonintact cells, respectively). Mineral coverages by intact and nonintact cells in the Mn-rich saprolite or ghost rindlet at 2.4 m depth, were significantly different from those observed in the topmost sample of lower saprolite (3.1 m), with p-values of 0.042 and 0.003, respectively ($\alpha = 0.050$). Mineral coverage by nonintact cells also differed between upper saprolite (2.0 m) and Mn-rich saprolite at 2.4 m (p-value of 0.010), clearly distinguishing the "ghost rindlet" from the upper and lower saprolite sections. Due to high variability of mineral surface coverages in each field of view, the mean %MAC values were not statistically different from each other throughout the lower saprolite (3.1-4.7 m) (Table 1).

Mineral and cell areas were normalized to values per 100,000 μm^2 of field of view to account for differences in total surface areas examined at each depth (Table 1). Normalized areas of intact cells were greatest in soils at 0.15 and 0.31 m (ca. 5,000 μm^2), decreased to 1,300 μm^2 or less in the upper saprolite (1.5-2.4 m), and remained less than 500 μm^2 throughout the lower saprolite (Fig. 3a). In lower saprolite, the normalized area for intact cells was greatest near the saprock (401 μm^2 at 4.6 m). The gross pattern of change in nonintact cell area was similar to that for intact cell area, though nonintact cell areas were always higher in magnitude except at 4.6 m (Fig 3a insert). Respective normalized values for nonintact cell areas in soil, upper saprolite, Mn-rich saprolite, and lower saprolite, respectively, were ca. 12,000 μm^2, 2300-5600 μm^2, 4200 μm^2 and < 1000 μm^2 (Fig. 3a). In lower saprolite, nonintact cell area was highest at 4.4 and 4.7 m, i.e., near the saprock (773 and 751 μm^2, respectively) (Fig. 3a insert).

Normalized areas for each of the three mineral classes (values per 100,000 μm^2 of microscope field) showed that mixed opaque minerals represented the dominant mineral class in the soil and upper saprolite (ranging from 19,000 – 32,000 μm^2.) In the soil, normalized area for biotite was lower (4500 – 5000 μm^2) than it was for quartz (5400 – 5700 μm^2), consistent with weathering of this mineral occurring in surface soil (Murphy et al. 1998). In upper saprolite, biotite area was higher (13,000 – 17,000 μm^2) compared to the biotite area in soil. In the "ghost rindlet" and lower saprolite, biotite area was higher than in the two sections above it (Fig. 3b). In the lower saprolite, biotite area was highest at 4.4 and 4.6 m (56,000 and 43,000 μm^2 respectively), but was lower at 4.7 m near the saprock (12,000 μm^2). Quartz area (μm^2) varied little throughout the regolith profile (Fig. 3b).

Linear regression analyses of cell areas vs. mineral areas measured in individual images were performed for the three mineral classes (Fig 4). When expressed as area per 100,000 μm^2 FOV, mixed opaque minerals showed the highest coefficients of determination for both intact and nonintact cells, R^2 = 60 and 58%, P = 0.003 and 0.004, respectively (Fig. 4a). When areas for the two soil depths were excluded from the analysis, the relationship between intact cells and the mixed opaque mineral class was still observed, with R^2 value of 83% and p-value of <0.001; on the other hand, a significant relationship between mixed opaque minerals and nonintact cells was not found (R^2 = 34%, P= 0.076).

A weak negative relationship was observed between normalized biotite and cell areas (R^2 = 40% and P-value of 0.027 for intact cells and R^2 = 48 and P-value of 0.012 for nonintact cells; Fig 4b). However, this relationship was not observed when values from the two soil samples were removed from the dataset (P = 0.285 and 0.147 for intact and nonintact cells, respectively). When only the saprolite samples below 3 meters (3.1-4.9 m) were analyzed, linear regression analysis indicated no relationships between intact or nonintact cell areas versus areas for any of the mineral classes. No relationships were observed between normalized quartz and cell areas (Fig. 4c). Overall, results confirmed a positive relationship between microbial cells and the surfaces of mixed opaque minerals.

Bacterial community composition in deep regolith

Cloned 16S rRNA gene sequences from saprolite (4.6 and 4.7 m) and saprock (4.9 m) were highly diverse. A total of 269 sequences from all six libraries could be assigned to 13 divisions (>0.80 rRNA similarity) using Greengenes (DeSantis et al., 2006a and 2006b): *Proteobacteria, Acidobacteria, Firmicutes, Actinobacteria, Bacteroidetes, Cyanobacteria, Nitrospirae, Planctomyces, Thermus/Deinococcus, Verrucomicrobia, Chloroflexi,*

Synergistes, and *Aquificales* (Fig. 5). Sequences representing six to nine divisions were recovered from each library, with four divisions found in all six libraries (*Proteobacteria*, *Acidobacteria, Firmicutes,* and *Actinobacteria,* Suppl. Table 1). Combined representation of these four divisions accounted for 92-94% and 80-90% of all sequences in libraries from the north and south boreholes, respectively.

Coverage estimates for the three libraries from the north borehole samples were 65, 15, and 53% for 4.6, 4.7, and 4.9 m depths, respectively. Coverage estimates for corresponding sample depths in the south borehole were 48, 36, and 59% (Table 2.) The lowest observed coverage (15%) could have been related to the presence of a large number of sequences having 0.94-0.99 similarities to *Stenotrophomonas maltophilia* (16 of 33 sequences) in the LG-1N 4.7-m library. The only other library containing similar sequences was from the 4.9-m sample in the north borehole (10 of 61 sequences). Highly similar sequences have been detected in coal-mine drainage sites (Nicomrat et al. 2008) and ferromanganese-rich mineral deposits in caves (Northup et al. 2003). It should be noted that *Stenotrophomonas*-related sequences have been reported as suspected experimental contaminants, possibly from DNA extraction reagents (Tanner et al., 1998). In our study, it was unlikely that *Stenotrophomonas*-related sequences were contaminants because they were recovered in only two libraries, each derived from metagenomic DNA extracted by different procedures. In addition, sequences with 0.99 similarity to *S. maltophilia* were recovered from reverse-transcribed rRNA extracted from deep LG-1N samples (unpublished results). Cultivation of *S. maltophilia* from Fe-rich environments in other studies supports the finding that *S. maltophilia* or its close relatives are actual members of these deep regolith communities (Emerson and Moyer, 1997).

Statistical analyses of the six bacterial clone libraries collected from LG-1 N and LG-1 S (Fig. 5) showed that all but two of the 15 pairwise comparisons of library compositions were statistically different from each other (p-value $\leq$ 0.0017). For the LG-1 N series, libraries from the deeper 4.7-m saprolite and 4.9-m saprock were similar to each other but different from the 4.6-m saprolite. For the LG-1S series, saprolite libraries (4.6 m and 4.7 m) were similar to each other but distinct from the saprock library (4.9 m). For both boreholes, therefore, the two statistically similar libraries were obtained from adjacent regolith sections.

Clone libraries from the north and south boreholes differed with respect to their most abundant bacterial divisions. In LG-1 N libraries, sequences related to *gamma-Proteobacteria* dominated at all three depths (31%, 61%, and 30% of library sequences at 4.6, 4.7, and 4.9 m, respectively) (Fig. 5). In contrast, LG-1S libraries were dominated by sequences related to *Firmicutes* (33% and 67%, respectively, at 4.6 and 4.9 m) and to *Acidobacteria* (51% at 4.7 m depth). Five of six libraries contained sequences closely related to *Burkholderiales* having RDP similarities ranging from 0.94-0.99. Nearly all sequences with similarities >0.97 were affiliated with bacteria known to have heterotrophic metabolisms, including those with reported iron-acquisition capabilities (Suppl. Table 1). All six libraries contained sequences closely related to *Pseudomonas* spp., cultured representatives of which are known to produce siderophores under Fe-limiting conditions (Cox et al. 1981). Saprock from the north borehole contained two beta-Proteobacteria sequences having > 0.99 similarity to *Janthinobacterium* spp., another group of siderophore-producing heterotrophs (Uroz et al., 2009). One other sequence from saprock had 0.97 similarity to *Ralstonia*-related sequences recovered from granite-fracture water (Sahl et al. 2008) and iron-reducing media (Lin et al., 2007). Only one sequence was recovered (from

LG-1N, 4.6 m) which could be ascribed to lithoautotrophic bacteria. This sequence had 0.99 BLAST similarity to *Acidithiobacillus ferrooxidans* (HQ445627), the Fe(II)-oxidizer found frequently in acid mine drainage environments (Johnson and Hallberg 2003). Recovery of this sequence was of particular note because *A. ferrooxidans* is also capable of fixing N_2 and could thus represent a source of assimilable N in deep regolith (Valdes et al., 2009).

Differences between the bacterial communities in north and south boreholes were also reflected in divisions represented exclusively in one borehole. A single sequence related to *Thermus/Deinococcus* (HQ445740 with 0.98 similarity) was found among the LG-1 N libraries (Suppl. Table 1). Other rarer sequences found only in LG-1 S libraries were related to *Planctomyces* (HQ445695) *Verrucomicrobia* (HQ445668), *Chloroflexus* (HQ445691), *Synergistes* (HQ445687, -746, -875), and *Aquificales* (HQ445884) with 0.79-0.83 similarities. Not only were some divisions specific to one borehole, several classes and families within divisions were also exclusively found in one borehole. Among delta *Proteobacteria* representatives, sequences related to *Desulfuromonadales* were recovered from the north borehole, while *Myxococcales*-related sequences were found only in the south borehole.

Low RDP similarities of many sequences reflected a high degree of uncharacterized diversity in deep regolith. Sequences classified as *Clostridia* or unclassified *Firmicutes* had lower similarities (0.75-0.92) than sequences classified as *Bacilli* (0.92-0.99) (Suppl. Table 1). Sixteen of 35 *Firmicutes*-related sequences in saprock from the south borehole were classified as *Thermolithobacteria* with 0.80-0.83 similarities. The only cultured representatives of this newly established class of *Firmicutes* are thermophilic anaerobes isolated from hot springs (Sokolova et al., 2007). Nine other *Firmicutes* related sequences

from the south borehole had 0.96 similarity to GenBank accessions from wind deposited soils (Talera et al., 2008).

Pairwise BLAST analyses of several *Acidobacteria* sequences from the south borehole revealed these to have high rRNA similarities to cultured representatives such as *Acidobacterium capsulatum* (95%) and three others with recently sequenced genomes, *Solibacter* (94%), *Terriglobus* spp. and *Candidatus Koribacter* (92%), respectively (Ward et al. 2009). However, the majority of Acidobacteria-related sequences were unclassified with RDP similarities <0.90.

DISCUSSION

In a first attempt of its kind, we developed a procedure to track microbe-mineral associations in regolith using CLSM imaging, BacLight nucleic acid staining, and software tools. Previous mineralogical studies of Guaba Ridge saprolite established the presence of only two major primary minerals, quartz and biotite (Murphy et al. 1998; White et al. 1998). Because quartz and biotite in DIC images could be distinguished by light transmission and large grain sizes, we were able to estimate the relative proportions of these mineral surfaces with depth, designating all other mineral surfaces as "unidentified opaque." Surface area coverages (%MAC) by intact and nonintact cells were then calculated for each mineral class.

As expected, we observe higher %MACs in surface soils due to the presence of living roots, organic matter, and other plant-derived nutrients. In upper saprolite, we expected to observe lower %MAC values for intact and nonintact cells than in surface soils, since a hundredfold lower microbial densities were observed previously in samples from corresponding depths. At the intermediate depth of 2.4 m, where the darker, Mn-rich ghost rindlet was found, the %MAC value for nonintact cells was higher relative to values in the

more shallow saprolite (Table 1). Buss et al. (2005) recorded a similar increase in cell number at 2.2 m, where weight percentages of biotite, quartz, kaolinite, and Fe(II) and Mn(II) oxides were also higher compared to surrounding saprolite (Schulz and White 1999). The ghost rindlet layer thus appears to be a richer nutrient source that could support higher numbers of microorganisms at this depth.

In CLSM images of 4.7-m saprolite (deepest saprolite collected prior to saprock transition), biotite was the dominant mineral observed, and nonintact cell coverage increased to 5.9% MAC (Table 1). We interpreted this increase as a loss of cell viability as the availability of mineral-derived nutrients declined upon weathering. Although biofilm bacteria dependent on nutrient acquisition from minerals would be less likely to maintain viability as weathering progresses, other organisms may be able to sustain their activities by obtaining electron donors from necromass. Frequent observations of single intact cells in the midst of nucleic-acid-rich biofilms in our CLSM images (Fig. 2) support this interpretation.

Despite the predominance in our clone libraries of rRNA sequences affiliated with heterotrophic bacteria, little organic carbon is available to support heterotrophic activity in deep regolith. Organic carbon contents measured previously in Guaba Ridge regolith from 4.6 and 4.9 m depths were 0.19 and 0.09 wt %, respectively (Buss et al. 2005). One explanation for the presence of highly diverse heterotrophic bacterial rRNA sequences in deep regolith is the accumulation and persistence of nonviable or inactive heterotrophs following downward translocation from more organic-rich surface soils. If this explanation is correct, dead cells could serve as a nutrient source enabling a low level of metabolic activity by better-adapted organisms having one or more selective advantages. Significant differences in clone library compositions were observed between regolith samples collected from

boreholes separated by 1.5 m. Such differences could reflect spatial variability in precipitation-driven translocation of cells from surface soils. Variability in the kinds of cells that reach deep regolith from the surface could therefore influence the successional trajectories and eventual compositions of bacterial communities developing from species introduced earlier.

We have proposed that an important electron donor in this environment is Fe(II) derived from initial biotite weathering in rindlets and from hornblende weathering in saprock. In deep regolith, Fe(II)-oxidizing lithoautotrophs would therefore have the selective advantage of being able to use Fe(II) for energy and reducing power from primary minerals. Evidence for biological Fe(II) oxidation in Rio Icacos saprock includes measurements of lighter Fe isotope values, δ^{56}Fe = -0.40‰, which are consistent with biological activity (Buss et al., 2008; Buss et al., 2010). In addition, hornblende dissolution rates have been calculated to be 6 x 10^{-13} mol hornblende m^{-2} s^{-1}, and this would provide enough Fe(II) as a potential electron donor for a detectable, steady-state population of Fe(II)-oxidizers (Buss et al. 2008). Mixotrophs would have an additional advantage of being able to supplement inorganic electron donors with reduced carbon from necromass.

Acidity generated by Fe(II) oxidation also would lead to enhanced mineral dissolution, which would increase fluxes of Fe(II) and other nutrients from weathering minerals. The macronutrient potassium is released from biotite and feldspar, while phosphorus is released from apatite. The supply of nitrogen, probably the most limiting macronutrient in deep regolith, could be derived in part by bacteria capable of N_2 fixation, although the high energy demands of this process would require an adequate supply of electron donors. Gravimetric moisture contents of deep saprolite on Guaba Ridge, observed

between 28-34% (Buss et al. 2005), indicate that water would not be a factor limiting bacterial activity and nutrient acquisition.

In our proposed model for Rio Icacos regolith weathering, abiotic reactions still account for all initial weathering alterations in bedrock. In unfractured bedrock below the rindlet zone, abiotic Fe(II) oxidation in biotite was observed to occur and was attributed to O_2 diffusion into the low porosity bedrock (Fletcher et al., 2006; Buss et al. 2008). Oxidation of structural Fe(II) alters the layer silicate charge of biotite and affects the strength of interlayer bonding of K^+ cations. Biotite alteration in unfractured bedrock is accompanied by the formation of larger cracks that create rindlets, as well as smaller micro-cracks, which are found throughout the rindlet zone and saprock layer. Biotite oxidation was found to be complete in outermost rindlets (Buss et al. 2008). Such micro-cracks undoubtedly promote increased porosity and weathering of other primary minerals including hornblende, plagioclase, and apatite to release the nutrients Mg^{2+}, K^+, Ca^{2+} and PO_4^{2-}. These nutrients could support biological oxidation of aqueous or exchangeable Fe(II) from hornblende, which weathers completely within the even more porous saprock layer.

As hornblende, feldspar, and apatite dissolve at the bedrock-saprolite interface, many cells immobilized in biofilms on biotite surfaces would eventually die as nutrient availability declined. Dead biofilms and secondary mineral coatings on biotite could explain the slowed weathering and persistence of primary biotite grains throughout the entire saprolite layer (Murphy et al. 1998). Detection of DNA sequences associated with Fe(II)-oxidizing and siderophore-producing bacteria is consistent with the proposed importance of Fe(II) as an electron donor in deep regolith. Enhanced mineral dissolution resulting from activity of heterotrophic bacteria such as *Bacillus* spp. and *S. maltophilia* could increase electron donors

Fe(II) oxidizers and other nutrients for community members. Subsequent development of diverse and spatially distinct communities could be due to chance translocations of microorganisms from surface soils, adaptive cooperation between lithoautotrophs and heterotrophs, and reutilization of dead biomass to maintain microbial viability.

Despite the low-nutrient environments provided by deep regolith in comparison to surface soils, biogeochemical processes in deep regolith can generate positive feedbacks that promote weathering. Since the DNA used to construct clone libraries in the present study could have been derived from moribund bacteria, construction of clones or metagenomic libraries from RNA, rather than DNA, would be more informative in identifying actively metabolizing populations. We are just beginning to understand the relationships between subsurface microorganisms and their low-nutrient environments. Future studies employing *in situ* and RNA-based analyses of active metabolisms and the nutrient sources supporting them will enhance our understanding of the mechanisms by which microorganisms contribute to bedrock weathering.

Acknowledgments

We thank J. Williams for field support; N. Zembower, E. Kunze, and S. Magargee from the Huck Institute's Cytometry lab for assistance with the CLSM; and D. Grove at the Genomics Core Facility. Research was funded by DOE grant DE-FG02-05ER15675, with some logistical support contributed by the NSF-supported Luquillo Critical Zone Observatory (EAR 0722476). M. L. Minyard acknowledges fellowship support from the Penn State Biogeochemical Research Initiative for Education (BRIE, NSF-IGERT grant DGE-9972759) and the DoD Science Mathematics and Research for Transformation (SMART) Program.

REFERENCES

Altschul SF, Gish W, Miller W, Myers EW, Lipman DJ. 1990. Basic local alignment search tool. Journal of Molecular Biology 215: 403-410.American Geological Institute. 1976. Dictionary of Geological Terms: Anchor Press.

Braun J-J, Remy J, Ngoupayou N, Viers J, Dupre B, Bedimo, J-P B, Boeglin J-L, Robain H, Nyeck B, Freydier R, Sigha Nkamdiou L, Rouiller J, Muller J-P. 2005. Present weathering rates in a humid tropical watershed: Nsimi, South Cameroon. Geochim. Cosmochim. Acta 69: 357-387.

Brown S, Lugo AE, Silander S, Liegel L. 1983. Research history and opportunities in the Luquillo Experimental Forest. USDA Forest Service General Technical Report: p.44.

Buss HL, Bruns MA, Schultz MJ, Moore J, Mathur CF, Brantley SL. 2005. The coupling of biological iron cycling and mineral weathering during saprolite formation, Luquillo Mountains, Puerto Rico. Geobiology 3: 247-260.

Buss HL, Mathur R, White AF, Brantley SL. 2010. Phosphorous and iron cycling in deep saprolite Luquillo Mountain, Puerto Rico. Chemical Geology 269: 52-61.

Buss HL, Sak PB, Webb SM, Brantley SL. 2008. Weathering of the Rio Blanco quartz diorite, Luquillo Mountains, Puerto Rico: Coupling oxidation, dissolution, and fracturing. Geochimica et Cosmochimica Acta 72: 4488-4507.

Cole JR, Wang Q, Cardenas E, Fish J, Chai B, Farris RF, Kulam-Syed-Mohideen AS, McGarrell DM, Marsh T, Garrity GM, Tiedje JM. 2009. The Ribosomal Database Project: improved alignments and new tools for rRNA analysis. Nucl. Acids Res. 37 (suppl 1): D141-D145.

Cox CD, Rinehart KL, Moore ML, Cook JC. 1981. Pyochelin: Novel structure of an iron-chelating growth promoter for *Pseudomonas aeruginosa*. Proc. Natl. Acad. Sci 78: 4256-4260.

DeSantis TZ, Hugenholtz P, Keller K, Brodie EL, Larsen N, Piceno YM, Phan R, Anderson GL. 2006a. NAST: a multiple sequence alignment server for comparative analysis of 16S rRNA genes. Nucleic Acids Research 34: 394-399.

DeSantis TZ, Hugenholtz P, Larsen N, Rojas M, Brodie EL, Keller K, Huber T, Dalevi D, Hu P, Andersen GL. 2006b. Greengenes, a Chimera-Checked 16S rRNA Gene Database and Workbench Compatible with ARB. Applied and Environmental Microbiology 72: 5069-5072.

Dong H, Peacor DR, Murphy SF. 1998. TEM study of progressive alteration of igneous biotite to kaolinite throughout a weathered soil profile. Geochimica et Cosmochimica Acta 62: 1881-1887.

Emerson D, Moyer C. 1997. Isolation and characterization of novel iron-oxidizing bacteria that grow at circumneutral pH. Applied and Environmental Microbiology 63: 4784-4792.

Fletcher R, Buss HL, Brantley SL. 2006. A spheroidal weathering model coupling porewater chemistry to soil thickness during steady-state denudation. Earth and Planetary Science Letters 244: 444-457.

Fritz SJ, Ragland PC. 1980. Weathering rinds developed on plutonic igneous rocks in the North Carolina Piedmont. American Journal of Science 280: 546-559.

Heydorn A, Nielsin AT, Hentzer M, Sternberg C, Givskov M, Ersboll BK, and Molin S. 2000. Quantification of biofilm structures by the novel computer program COMSTAT. Microbiology 146: 2395-2407.

Johnson DB, Hallberg, KB. 2003. The microbiology of acidic mine waters. Res Microbiology 154: 466-473.

Lane DJ. 1991. 16S/23S rRNA sequencing. In: Stackebrandt E, Goodfellow M, editors. Nucleic Acid Techniques in Bacterial Systematics. New York: John Wiley & Sons.

Larsen MC, Collar PD, Stallard RF. 1993. Research plan for the investigation of water, energy, and biogeochemical budgets in the Luquillo Mountains, Puerto Rico. USGS Open File Report: 92-150.

Leuko S, Legat A, Fendrihan S, Stan-Lotter H. 2004. Evaluation of the LIVE/DEAD *Bac*Light kit for detection of extremophilic archaea and visualization of microorganisms in environmental hypersaline samples. Appl Environ Microbiol 70:6884-6886.

Lin B, Roling WFM, van Breukelen BM. 2007. Iron-reducing microorganisms in a landfill leachate-polluted aquifer: complementing culture-independent information with enrichments and isolations. Geomicrobiology Journal 24: 283-294.

McDowell WH, Asbury CE. 1994. Export of carbon, nitrogen, and major ions from three tropical montane watersheds. Limnol. Oceanogr. 39:111-125.

Murphy SF. 1995. Weathering of biotite in a tropical forest soil, Luquillo Mountains, Puerto Rico. Thesis, Penn State University, University Park, PA.

Murphy SF, Brantley SL, Blum AE, White AF, Dong H. 1998. Chemical weathering in a tropical watershed, Luquillo Mountains, Puerto Rico: II. Rate and mechanism of biotite weathering. Geochimica et Cosmochimica Acta 62: 227-243.

Murray RGE, Doetsch RN, Robinow CF. 1994. Determinative and cytological light microscopy, In: Gerhardt P, editors. Methods for General and Molecular Bacteriology, Washington, DC: American Society for Microbiology.

Nicomrat D, Dick WA, Dopson M, Tuovinen OH. 2008. Bacterial phylogenetic diversity in a constructed wetland system treating acid coal mine drainage. Soil Biology and Biochemistry 40: 312-321.

Northup DE, Barns SM, Yu LE, Spilde MN, Schelble RT, Dano KE, Crossey LJ, Connolly CA, Boston PJ, Natvig DO, Dahm CN. 2003. Diverse microbial communities inhabiting ferromanganese deposits in Lechuguilla and Spider Caves. Environmental Microbiology 5: 1071-1086.

Sahl, J.W., R. Schmidt, E.D. Swanner, K.W. Mandernack, A.S. Templeton, T.L. Kieft, R.L. Smith, W.E. Sanford, R.L. Callaghan, J.B. Mitton, and J.R. Spear. 2008. Subsurface microbial diversity in deep-granitic-fracture water in Colorado. Applied and Environmental Microbiology 74:143-152.

Schloss PD, Westcott SL, Ryabin T, Hall JR, Hartmann M, Hollister EB, Lesniewski RA, Oakley BB, Parks DH, Robinson CJ, Sahl JW, Stres B, Thallinger GG, Van Horn DJ, Weber CF. 2009. Introducing mothur: Open-source, platform-independent, community-supported

software for describing and comparing microbial communitites. Applied and Environmental Microbiology 75: 7537-7541.

Schulz MS, White AF. 1999. Chemical weathering in a tropical watershed, Luquillo Mountains, Puerto Rico III: Quartz dissolution rates. Geochimica et Cosmochimica Acta 63: 337-350.

Seiders VM. 1971. Cretaceous and lower tertiary stratigraphy of the Gurabo and El Yunque quadrangles, Puerto Rico. In: USGS. U.S. Geological Survey Bulletin No. 1294: F1-F53.

Sokolova T, Hanel J, Onyenwoke RU, Reysenbach A-L, Banta A, Geyer R, Gonzalez JM, Whitman WB, Weigel J. 2007. Novel chemolithotrophic, thermophilic, anaerobic bacteria *Thermolithobacter ferrireducens* gen. nov., sp. nov. and *Thermolithobacter carboxydivorans* sp. nov. Extremophiles 11:145-157.

Stonestrom DA, White AF, Akstin KC. 1998. Determining rates of chemical weathering in soils-solute transport versus profile evolution. Journal of Hydrology 209: 331-345.

Tanner MA, Goebel BM, Dojka MA, Pace NR. 1998. Specific ribosomal DNA sequences from diverse environmental settings correlate with experimental contaminants. Appl. Environ. Microbiol. 64:3110-3113.

Tarlera S, Jangid K, Ivester AH, Whitman WB, Williams MA. 2008. Microbial community succession and bacterial diversity in soils during 77000 years of ecosystem development. FEMS Microbial Ecology 64: 129-140.

Turner BF, Stallard RF, Brantley SL. 2003. Investigations of in situ weathering of quartz diorite bedrock in the Rio Icacos basin Luquillo Experimental Forest, Puerto Rico. Chemical Geology 202: 313-341.

Uroz S, Calvaruso C, Turpault MP, Sarniguet A, de Boer W, Leveau JHJ, Frey-Klett P. 2009. Efficient mineral weathering is a distinctive functional trait of the bacterial genus

Collimonas. Soil Biology Biochemistry 41:2178-2186.

USDA-NCRS. 2002. Soil survey of Caribbean National Forest and Luquillo Experimenal Forest, commonwealth of Puerto Rico. In: USDA editors. Natural Resources Conservation Service.

Valdes J, Pedroso I, Quatrini R, Dodson RJ, Tettelin H, Blake II R, Eisen JA, Holmes, DS. 2008. *Acidithiobacillus ferrooxidans* metabolism: from genome sequence to industrial applications. BMC Genomics 9: 597-621.

Ward NL, Challacombe JF, Janssen PH, Henrissat B, Coutinho PM, Wu M, Xie G, Haft DH, Sait M, Badger J, Barabote RD, Bradley B, Brettin TS, Brinkac LM, Bruce D, Creasy T, Daugherty SC, Davidsen TM, DeBoy RT, Detter JC, Dodson RJ, Durken AS, Ganapathy A, Gwinn-Giglio M, Han CS, Khouri H, Kiss H, Kothari SP, Madupu R, Nelson KE, Nelson WC, Paulsen I, Penn K, Ren Q, Rosovitz MJ, Selengut J, Shrivastava S, Sullivan SA, Tapia R, Thompson LS, Watkins KL, Yang Q, Yu C, Zafar N, Zhou L, and Kuske CR. 2009. Three genomes from the phylum *Acidobacteria* provide insight into the lifestyles of these microorganisms in soils. Appl. Environ. Microbiol. 75:2046-2056.

White AF, Blum AE. 1995. Effects of climate on chemical weathering in watersheds. Geochimica et Cosmochimica Acta 59: 1729-1747.

White AF, Blum AE, Schulz MS, Vivit DV, Stonestrom DA, Larsen M, Murphy SF, Eberl D. 1998. Chemical weathering in a tropical watershed, Luquillo Mountain, Puerto Rico: I. Long-term versus short-term weathering fluxes. Geochimica et Cosmochimica Acta 62: 209-226.

Zhou J, Bruns MA, Tiedje JM. 1996. DNA recovery from soils of diverse composition. Applied and Environmental Microbiology 62: 316-322.

FIGURE LEGENDS

Figure 1. Example of a 2-D display image from LG-1N saprolite (4.7-m depth) generated from a 132,400 μm^2 field-of-view at 400x (scale bars are 50 µm): **a and c)** fluorescence color display images generated with Ar and HeNe lasers, respectively, and used as input for manual threshold determinations in COMSTAT. The points of green fluorescence account for a very small percentage of area and are visible at the upper and lower right portions of the image 1a; **b and d)** COMSTAT-processed images showing white areas corresponding to fluorescent pixels from intact and nonintact cells in the previous two images after selecting optimized threshold values; **e)** DIC display image of mineral surfaces supporting cells; and **f)** input for ImageJ analysis showing manually selected areas for each of three mineral classes: quartz (Q); biotite (B), and mixed opaque minerals (M).

Figure 2. CLSM images of nonintact (red) and intact (green) microbial cells from 4.7 m depth (scale bars are 50 µm). **(a)** Three-channel display image combining views from DIC and both laser channels (Ar laser for SYTO 9 visualization of intact cells and HeNe laser for PI visualization of nonintact cells). **(b)** View showing association of intact and nonintact cells with fractured and opaque biotite (labeled B) and mixed opaque minerals (labeled as M). Few microbes were observed on the transparent quartz grains (labeled Q).

Figure 3. **(a)** Plot showing cell areas, normalized per 100,000 μm^2 of field-of-view (FOV), for intact (open squares) and nonintact (closed triangles) cells, with regolith depth on y-axis from 0 to 5 m; **(Insert)** Expanded view of the lower portion of plot (a) showing normalized cell areas between 3 and 5 m depth on y-axis. **(b)** Plot showing areas of each mineral class

calculated with ImageJ and normalized per 100,000 μm^2 of FOV, with regolith depth on y-axis from 0 to 5 m: biotite (gray squares); mixed opaque minerals (closed diamonds); and quartz (open circles).

Figure 4. **(a)** Linear regression plots of normalized CLSM data for intact and nonintact cell areas (μm^2 normalized per 100,000 μm^2 of FOV) vs. mixed opaque mineral areas (μm^2 per 100,000 μm^2 of FOV) reveals a positive relationship between mixed minerals and cell area. **(b)** Linear regression plot of normalized CLSM data for intact and nonintact cell areas (μm^2 normalized per 100,000 μm^2 of FOV) vs. biotite mineral areas (μm^2 per 100,000 μm^2 of FOV) reveals a weak negative relationship between biotite and cell area. **(c)** Plot of normalized CLSM data for intact and nonintact cell areas (μm^2 normalized per 100,000 μm^2 of FOV) vs. quartz mineral areas (μm^2 per 100,000 μm^2 of FOV). A relationship was not observed between quartz and cell area.

Figure 5. Bar charts showing proportional representation of bacterial divisions, as determined using classification tools in Greengenes, in six 16S rRNA clone libraries generated from DNA extracts. of LG-1 North (left) and LG-1 South (right). Bar charts for libraries from LG-1 North (left) and LG-1 South (right) are shown for saprolite (4.6- and 4.7 m) and saprock (4.9 m). The classes of *Proteobacteria* are represented with the bacterial divisions. Divisions with a low number of representatives are designated as “other”.

Table 1. Confocal laser-scanning microscopy (CLSM) data collected from LG-1 N and LG-1 S regolith boreholes

Depth (m)	Rego-lith layer	Descrip-tion of regolith section used in text	£Total area of mineral surface (μm^2) exam-ined at each depth	tTotal area of intact cells (μm^2) exam-ined at each depth	tTotal area of nonintact cells (μm^2) exam-ined at each depth	ŧ Mean (± s.e) percentage of Mineral Area Covered (MAC) by intact cells per field of view	ŧ Mean (± s.e.) percentage of Mineral Area Covered (MAC) by nonintact cells per field of view	§Statistic al analysis (p-values) for %MAC of intact cells	§Statis-tical analysis (p-values) for %MAC of nonintact cells
0.15	Bw	Soil	333,286	54,984	125,017	16.8 ± 4.48	38.6 ± 8.36	-	-
0.31	Bw	Soil	620,225	55,040	137,439	9.4 ± 1.35	22.7 ± 5.57	0.149	0.141
1.5	C	Upper Saprolite	407,513	13,525	59,610	3.6 ± 1.28	17.04 ± 6.49	0.006*	0.515
2.0	C	Upper Saprolite	371,131	9,403	18,701	1.93 ± 0.82	4.10 ± 1.22	0.296	0.091
2.4	C	Ghost Rindlet	427,704	6,525	50,460	1.42 ± 0.58	14.0 ± 2.84	0.624	0.010*
3.1	C	Lower Saprolite	368,662	107	4,206	0.037 ± 0.011	1.94 ± 0.95	0.042*	0.003*
3.7	C	Lower Saprolite	92,906	375	824	0.439 ± 0.34	1.15 ± 0.06	0.272	0.493
4.0	C	Lower Saprolite	75,877	80	829	0.09 ± 0.023	1.19 ± 0.29	0.337	0.951
4.3	C	Lower Saprolite	78,546	125	505	0.2 ± 0.132	0.74 ± 0.268	0.441	0.276
4.4	C	Lower Saprolite	78,311	323	983	0.496 ± 0.454	1.50 ± 0.90	0.559	0.454
4.6	C	Lower Saprolite	91,489	680	501	0.88 ± 0.74	0.57 ± 0.178	0.664	0.357
4.7	C	Lower Saprolite	162,929	463	8,960	0.239 ± 0.092	5.94 ± 2.41	0.415	0.057

£ Total area of mineral surfaces (μm^2) examined equals the sum of mineral surface areas in all fields of view collected at a given depth.

t Total area of cells (intact and nonintact) equals the sum of all green- or red-fluorescing areas, respectively, in all fields of view collected at a given depth.

ŧ Mean %MAC is the mean mineral surface area covered by cells (Equation 1) averaged from all images collected at the corresponding depth ± the standard error.

§ p-values were determined using 2-sample t tests in Minitab software (State College, PA) (α = 0.05) to evaluate differences between %MAC values from CLSM data at a given depth and from the depth immediately above it. The p-values labeled with * indicate significant differences.

Table 2. 16S rRNA clone library data from deep saprolite and saprock collected from LG-1 N and LG-1 S boreholes

Depth (m)/core	LG-1 North			LG-1 South		
	OTU	Chao 1	% Coverage*	OTU	Chao 1	% Coverage*
4.6	21	32.1	65	32	66.5	48
4.7	16	107	15	29	79.6	36
4.9	33	61.9	53	22	37.6	59

*Percent coverage is an estimate value calculated from OTU/Chao 1

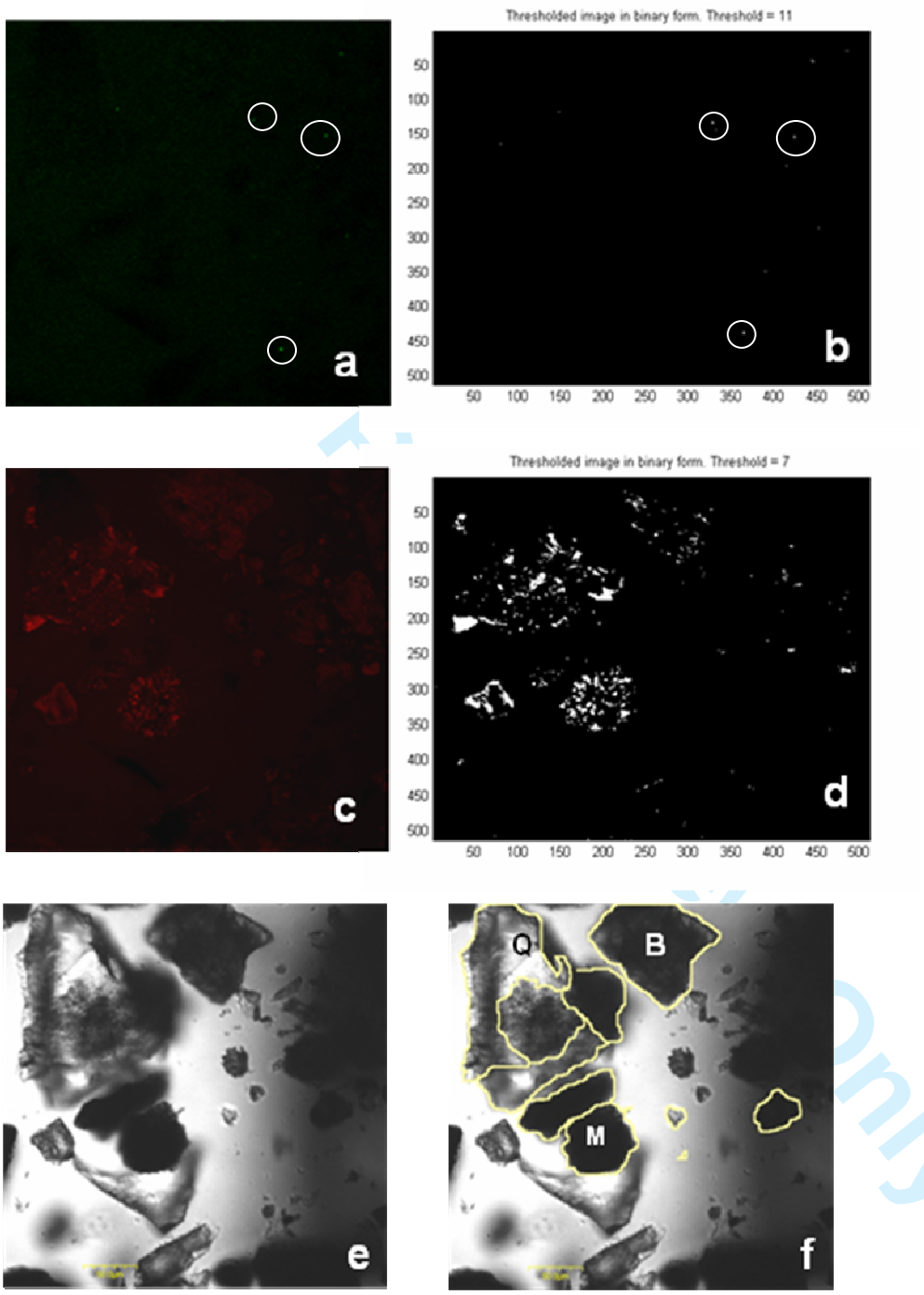
Thresholded image in binary form. Threshold = 11
Thresholded image in binary form. Threshold = 7
a
b
c
d
e
f
Q
B
M

Figure 1.

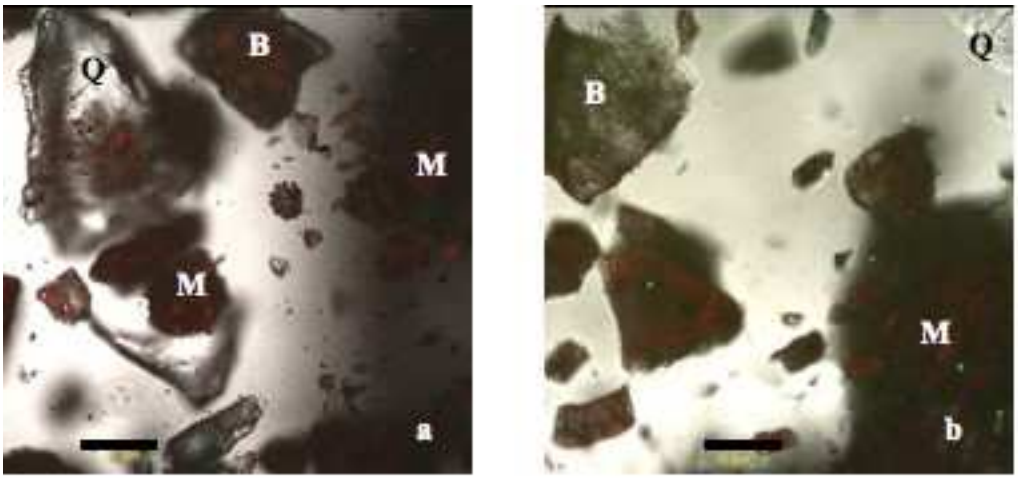

Figure 2.

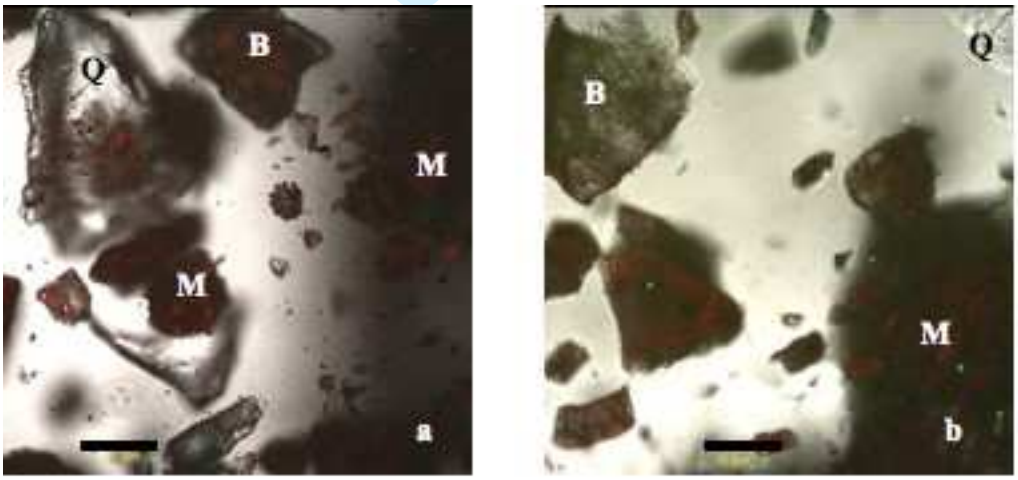

Figure 2.

Figure 3.

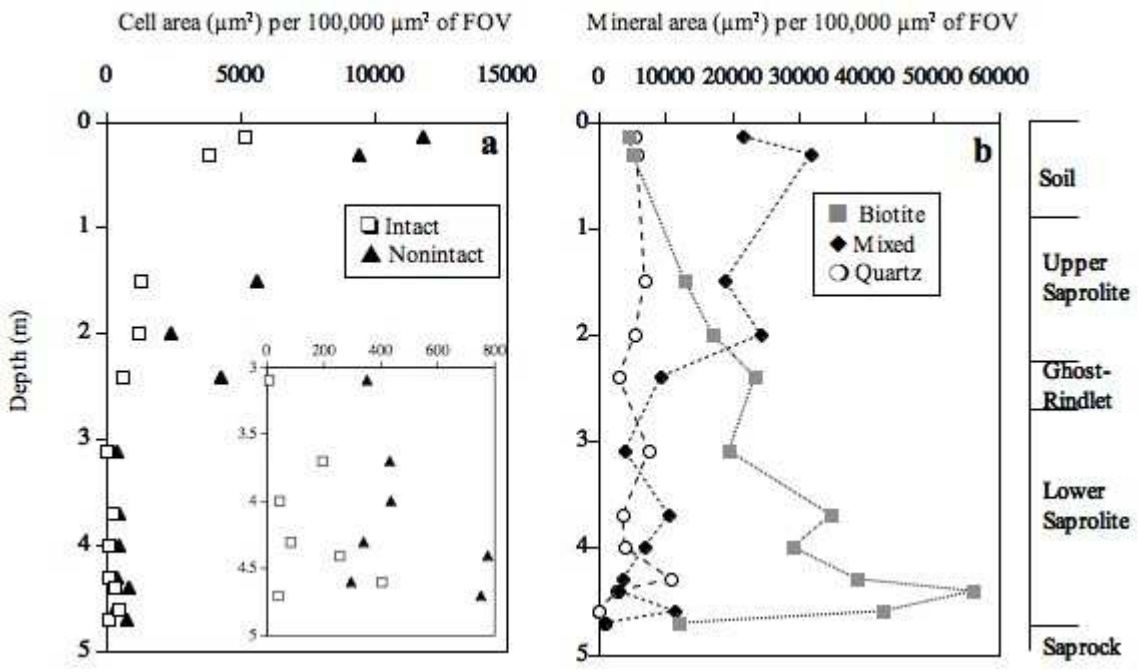

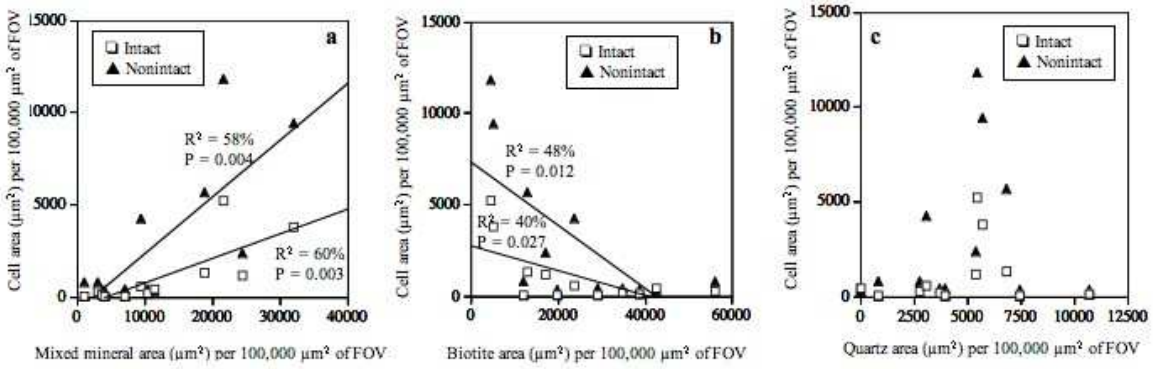

Figure 4.

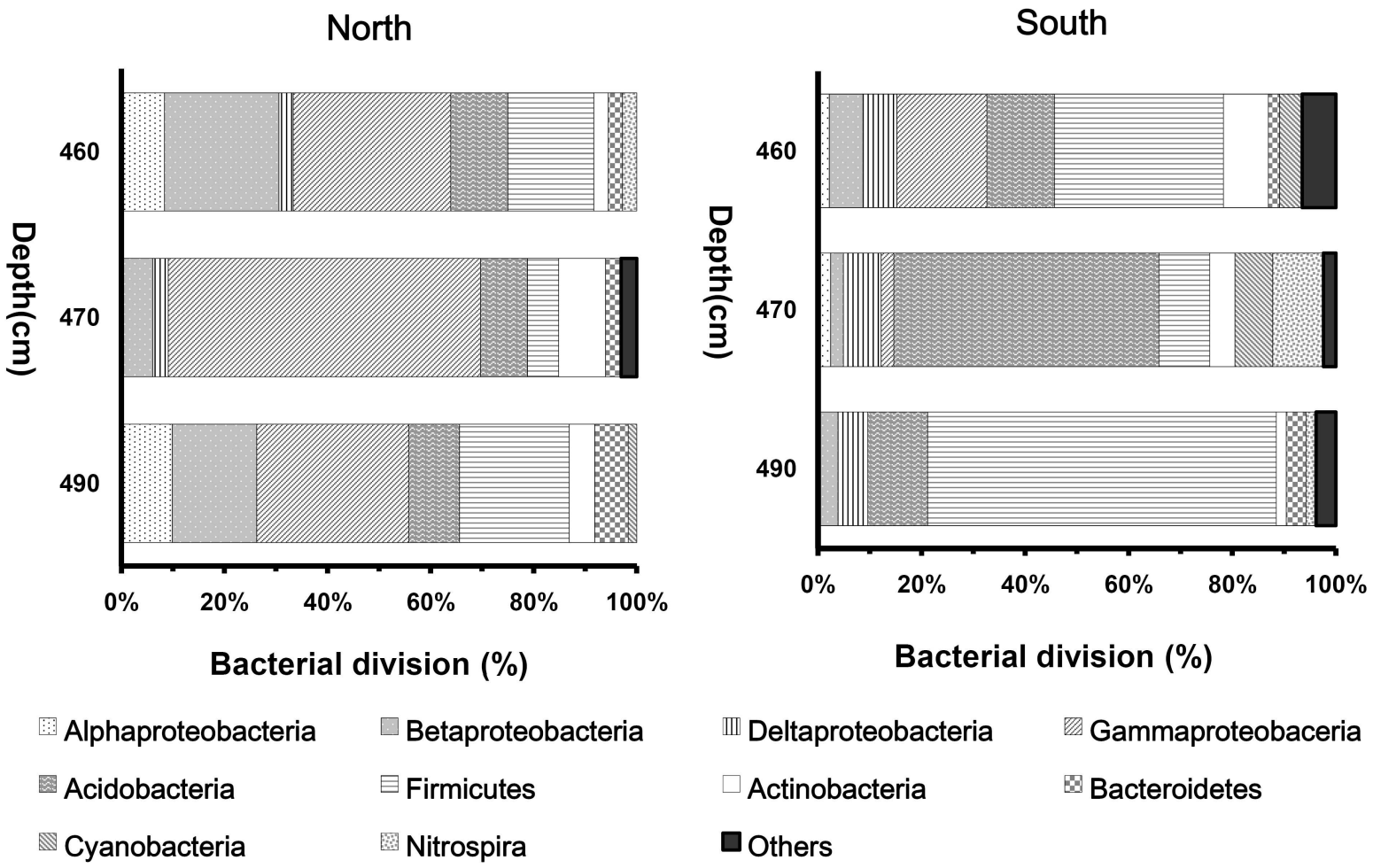
North
South
Depth(cm)
460
470
490
0%
20%
40%
60%
80%
100%
Bacterial division (%)
Alphaproteobacteria
Betaproteobacteria
Deltaproteobacteria
Gammaproteobaceria
Acidobacteria
Firmicutes
Actinobacteria
Bacteroidetes
Cyanobacteria
Nitrospira
Others

Figure 5.

Supplemental Figure 1. Cartoon depiction of soil/saprolite sample in a dual-chambered coverslip placed over the inverted objective of the confocal laser-scanning microscope.

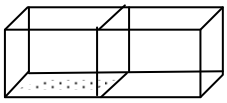

Chamber with coverslip on the bottom. An agarose suspension of saprolite grains covers the coverslip surface.

z

Inverted microscope objective with computer-controlled movement in vertical (z) direction